Supporting Information for

Origin of reversible photo-induced phase separation in hybrid perovskites

Connor G. Bischak[1], Craig L. Hetherington[1,2], Hao Wu[1,†], Shaul Aloni[3,4], D. Frank Ogletree[3,4], David T. Limmer[1,5], and Naomi S. Ginsberg[1,2,3,5,6.]*

[1]Department of Chemistry, University of California, Berkeley, California 94720, United States

[2]Molecular Biophysics and Integrative Bioimaging Division, Lawrence Berkeley National Laboratory, Berkeley, California, 94720, United States

[3]Materials Science Division, Lawrence Berkeley National Laboratory, Berkeley, California, 94720, United States

[4]Molecular Foundry, Lawrence Berkeley National Laboratory, Berkeley, California, 94720, United States

[5]Kavli Energy NanoScience Institute, Berkeley, California 94720, United States

[6]Department of Physics, University of California, Berkeley, California 94720, United States

*Correspondence to: nsginsberg@berkeley.edu

[†]Current address: Department of Chemistry and Chemical Biology, Harvard University, Cambridge, MA 02138, United States

Supporting Information contents:

1. Materials and methods
2. Explanation for why the electron beam does not cause demixing
3. Figures S1-S13
4. Videos S1-S6
5. Tables S1-S2
6. References

Materials and methods

Perovskite deposition and characterization

$MAPb(Br_xI_{1-x})_3$ was deposited via spin coating at 2000 rpm from 0.55 M solutions containing different ratios of $PbBr_2$ (Aldrich), CH_3NH_3Br (Dyesol) , PbI_2 (Aldrich), and CH_3NH_3I (Dyesol) in DMF (Aldrich). For CL and SEM imaging and *in situ* acquisition of PL spectra, films were deposited on Si substrates and annealed in air at 100 °C for 5 min. Films on Si were stored in N_2 prior to imaging. For confocal microscopy and PL spectra acquired outside of the SEM chamber, films were deposited on glass cover slips and annealed in air at 100 °C for 5 min. A thin (~0.5-1.0 μm) layer of poly(methyl methacrylate) (PMMA, Aldrich) in anisole (Aldrich) was spun onto the sample to protect them from moisture. All substrates were cleaned prior to perovskite deposition by sonicating in acetone (Aldrich) and isopropyl alcohol (Aldrich) for 5 min each followed by O_2 plasma cleaning in a reactive ion etch (RIE) for 5 min. $MAPb(Br_xCl_{1-x})_3$ films were made using an identical procedure, replacing DMF with dimethyl sulfoxide (DMSO), PbI_2 with $PbCl_2$ (Aldrich), and CH_3NH_3I with CH_3NH_3Cl (Dyesol).

$CsPb(Br_xI_{1-x})_3$ films were fabricated by making 0.3 M solutions of CsBr (Aldrich)/$PbBr_2$ and CsI (Aldrich)/PbI_2 in DMSO and then mixing these solutions in the appropriate ratio. Solutions were stirred for 1 h at 150 °C. Films were deposited on glass cover slips (prepared as described above) by filtering through a 0.2 μm filter and spin coating while keeping the solution at ~150 °C. All films were annealed at 75 °C for 10 min. A thin (~0.5-1.0 μm) layer of PMMA was spun onto the sample to protect them from moisture.

To confirm that the samples are of high quality, photoluminescence (PL) lifetime measurements were collected with a Horiba Jobin Yvon Fluorolog-3 Spectrofluorometer at a repetition rate of 1 MHz and a typical pulse width of < 1.2 ns using an attached 370 nm NanoLED (Horiba Scientific) as the time-correlated single-photon counting (TCSPC) source. Films composed of $MAPbBr_3$ had a lifetime of 25 ns, which is comparable to previously produced high quality films.[1] $MAPb(Br_{0.9}I_{0.1})_3$ films had a shorter lifetime (~5 ns) presumably due to the formation of iodide-rich clusters during the measurement,[1] which serve as trap sites and lower the PL lifetime.

Cathodoluminescence (CL) and scanning electron microscopy (SEM)

Cathodoluminescence (CL) and secondary electron (SE) images were acquired with a modified Zeiss Gemini SUPRA 55 S2 Scanning Electron Microscope (SEM). An aluminum parabolic reflector was positioned above the sample in order to couple a 1.3π sr solid angle of emission into a photomultiplier tube (Hamamatsu, H7421-40) outside of the vacuum chamber. A 405 nm LED (M405L2, Thorlabs) was used for *in situ* illumination and as the excitation source for the collection of PL spectra. All CL images were acquired by first blanking the electron beam, moving to the region of interest, and then recording an image. Light soaking and CL acquisition were alternated to acquire image series. All CL images were acquired with 512 x 512 pixels of a 10 μm x 10 μm field of view, a scan rate of 10 ms/line, a current of 50 pA, and an accelerating voltage of 3.0 kV. A 590 nm longpass filter was used during CL acquisition. Higher resolution SE images were acquired after CL

image acquisition with 1024 x 1024 pixels and a scanning rate of 20 ms/line. For CL and PL spectral acquisition, the SEM was fitted with a fiber-coupled QE65PRO spectrometer with a HC1-QE grating (Ocean Optics).

Confocal microscopy and photoluminescence (PL) spectra

Confocal microscopy images were collected with an IX83 inverted microscope (Olympus) using a 40x 0.95 NA objective. Images of the Br-rich and I-rich regions were acquired simultaneously using a 560 nm dichroic filter and grating set to 500-550 nm and 650-700 nm, for the Br-rich and I-rich regions, respectively. All images were acquired with 512 x 512 pixels with a 200 μm x 200 μm field of view and a scan rate of 10 ms/line. For the I-rich cluster stabilization demonstration (**Figure S5**), light soaking was induced with a 405 nm LED (M405L2, Thorlabs) at 100 mW/cm^2, an image was acquired with a 405 nm laser at, a 635 nm laser was positioned in the center of the field of view at 20.0 μW, and after five minutes another image was acquired with the 405 nm laser at 4.0 μW. For the film luminescence patterning demonstration (**Figure S6**), the film was constantly illuminated with a 660 nm LED (Thorlabs, M660L3) at 450 mW/cm^2. A 405 nm laser (350 nW) was used to induce halide phase separation locally for 2 min at each position. To probe the induced pattern, a 405 nm laser (4.0 μW) was used, scanning at 10 ms/line. PL spectra were acquired using a 405 nm LED (M405L2, Thorlabs) as the excitation source and a fiber-coupled QE65PRO spectrometer with a HC1-QE grating (Ocean Optics).

Intermolecular potential

The model we use to simulate the mixed halide hybrid perovskite borrows significantly from recent work by Mattoni et al.[2] and older work by Lewis and Catlow.[3] Specifically we adopt the mixed Lennard-Jones

$$U(r) = 4\epsilon \left[\left(\frac{\sigma}{r} \right)^{12} - \left(\frac{\sigma}{r} \right)^{6} \right]$$

and Buckingham

$$U(r) = Ae^{-r\rho} - \frac{C}{r^6}$$

form for the potentials with parameters taken for the methylammonium (MA) molecules, Pb^{2+} and I$^-$ ions from **Ref.** [2]. Lennard-Jones and Buckingham potentials were truncated and shifted at 10 Å, and long ranged electrostatics were computed with PPPM/Ewald. For simulations with Br$^-$ or Cl$^-$, we derive parameters from the I$^-$ interactions by scaling the size and in proportion to the ratio of the known ionic radii and used geometric mixing rules as proposed by **Ref.** [3]. **Table S1** summarizes the parameters used where H$_1$ refers to those hydrogens attached to the nitrogen and H$_2$ to those hydrogens attached to the carbon.

Simulation protocol

Simulations are run to sample an ensemble with constant temperature, T, pressure, p, and

chemical potential difference between two halide species, $\Delta\mu$. Constant temperature and pressure constraints are sampled using a Nose Hoover integrator with Parrinello-Rahman barostat[4] with 3 chains and 2 ps time constants suitable for a periodic system, and with the MA molecules held rigid following Zhang and Glotzer.[5] Grand canonical Monte Carlo moves are added on top of the molecular dynamics to sample different halide compositions, or to sample different configurations at fixed composition, with 500 trial particle swaps every 200 integration steps. In this way, properties dependent on various average compositions as well as the susceptibility to changes in concentration, can be probed. A time step of 2 fs was used and most sets of calculations were equilibrated for 50 ps, with initial geometries take from[6] and 10 ns were used to converge averages. Integration and force evaluation were accomplished with LAMMPS.[7]

Model validation and calculations and decomposition of the enthalpy of mixing

Using the model and simulation protocol described above, we have validated our model by computing the bulk lattice and elastic constants. Bulk moduli were computed for pure halide lattices by computing the compressibility from the mean squared volume fluctuations. This yielded 17.5, 17.4 and 15.4 GPa, for pure I, Br and Cl lattices. These are within 25% of experiment.[8] In addition, we have computed average lattices constants of 6.26 Å, 5.80 Å and 5.50 Å for pure I, Br and Cl lattices which are within 1% agreement with experiment.[9] Lattice constants as a function of composition are shown in **Figure S1** with linear interpolations between pure lattices.

Results for the average concentration as a function of chemical potential difference are shown in **Figure S1**. A reference value of 5.5 kcal/mol and 20 kcal/mol is used to place both curves on the same scale. These curves indicate that exchange between I⁻ and Br⁻ is continuous, though with a peak in susceptibility around $\Delta\mu=0$. This is consistent with the ground state stability of these mixtures. However, exchange between I⁻ and Cl⁻ appears discontinuous, with a jump in concentration around $\Delta\mu=0$, consistent with the observed instability of mixtures of these materials.

In order to understand the energetic driving forces for phase separation we have computed the enthalpy of mixing at fixed composition and either at fixed stress, 1 bar, or at fixed volume. We follow the procedure outlined above for the molecular dynamics simulations, and compute the enthalpy per unit cell as

$$\Delta H_{\mathrm{mix}}(x) = \langle H \rangle - x\big[\langle H(x=0) \rangle - \langle H(x=1) \rangle\big]$$

where x is the composition of the smaller halide in each mixture. The constant volume calculations are done with a volume fixed by linearly interpolating between the pure lattices. The results of these calculations are shown in **Figure S2** where the red data denotes constant strain and the blue constant stress. The shaded regions in those plots are fits to the Flory form,

$$\Delta H_{\mathrm{mix}}(x) = \chi x (1 - x)$$

4

which allows us to extract a critical demixing temperature, assuming a Flory-Huggins form for the free energy.

Extension to PIMD simulations and free energy calculations

To extend the molecular model to incorporate effects from photo-generated charges, we used a path integral molecular dynamics description on an excess charge following Refs 44 and 45, with pseudo potentials following **Ref.** [12]. The form of the pseudo potential consisted of simple Coulomb interactions for the excess electron and anionic species, and short-ranged truncated Coulomb interactions for the cations. The cut-off radii were chosen as the ionic radii of each species and reasonably recover the known ionization potentials for each cation. The values are summarized in **Table S2**. Ring polymers with 1024 beads were found to be sufficient to converge the average radius of gyration, and a fictitious mass of 1 amu was used in the calculations with a timestep of 0.5 fs.

Simulations with the excess charge were accomplished using the same procedure outlined above. To compute the free energies as a function of composition, simulations were run with $\beta\Delta\mu = \{-3,3\}$, in steps of 0.5. In the case of the excess charge, where nucleation barriers between iodide-rich and bromide-rich phases result in poor sampling near coexistence, replica exchange was performed by scaling the temperature associated with grand-canonical moves between 300 K-600 K in increments of 30 K. WHAM was used to combine the different ensemble calculations into a single free energy estimate,[13] reweighted to coexistence, with errors computed from standard bootstrapping. The binding energy is computed from the change in the average potential energy and the deformation size is computed from the radius of gyration of the ring polymer weighted by the electron phonon coupling.

Landau theory with strain and excess charge

We start by assuming that the phase separation between different halide species satisfies a Flory-Huggins solution theory,

$$H_c = \int_{\mathbf{r}} \chi \phi(\mathbf{r})[1 - \phi(\mathbf{r})] + T\{\phi(\mathbf{r}) \ln[\phi(\mathbf{r})] + [1 - \phi(\mathbf{r})] \ln[1 - \phi(\mathbf{r})]\}$$

where χ is related to the excess enthalpy of mixing, T is the temperature, and ϕ is the local concentration of iodide relative to bromide. Assuming that the light does not induce plastic deformations or other large scale morphological transitions the strain field can be assumed to be Gaussian,

$$H_l = \int_{\mathbf{r}} \mathbf{K}\,\Sigma^2(\mathbf{r})/2(1-\nu)$$

Here Σ is the local strain field, K is bulk modulus in the mixed phase and ν is Poisson's ratio. For simplicity the elasticity is assumed to be isotropic. To lowest order these fields are coupled with a bilinear term,

$$H_{c,l} = \int_{\mathbf{r}} c_2 \mathbf{\Sigma}(\mathbf{r}) \phi(\mathbf{r})$$

where the coupling coefficient c_2 is taken to be proportional to the change in lattice constants, a, with composition:[14]

$$c_2 = 2\eta K/(1-\nu)$$

where $\eta = d\ ln\ a/d\phi$ evaluated at $\phi=1/2$. This theory offers a complete description of the ground state free energy surface. Adding these three terms together, integrating out the strain fields and expanding ϕ around 0.5, a ϕ^4 theory is obtained,[15]

$$H = \int_{\mathbf{r}} m[\phi(\mathbf{r}) - 1/2]^2 + u[\phi(\mathbf{r}) - 1/2]^4$$

where $m=2T-\chi-2K\eta^2/(1-\nu)$, and $u=4T/3$. The free energy is determined by evaluating this Hamiltonian within mean field theory by finding solutions to the equation,

$$\frac{dH}{d\bar{\phi}(r)} = 0$$

that minimize the Hamiltonian. Then the per unit cell free energy is

$$\Delta F(x) = H[\bar{\phi}].$$

For Br/I mixtures, m is taken from the molecular dynamics simulations and set to $m=2T(K)-390K$.

In order to describe light-induced phase separation an additional term reflecting the electronic degrees of freedom must be added. We do this following the deformation potential theory for electron-phonon interactions[16], and make a semiclassical approximation to decouple the electronic and ionic motions[17]. Specifically we add the lowest order coupling between excess charge density and the strain and composition fields,

$$H_{e,l-c} = \int_{\mathbf{r}} \alpha \mathbf{\Sigma}(\mathbf{r})|\Psi(\mathbf{r})|^2 + \epsilon\phi(\mathbf{r})|\Psi(\mathbf{r})|^2$$

where α is the dimensionless electron-phonon coupling constant and $\epsilon<0$ is the energetic bias of an excess charge to reside on the Iodide rich regions. $|\Psi|^2$ is the excess charge density localized to a region l^3. The kinetic energy of the electrons has been neglected. This additional term in the Hamiltonian is linear and permits the strain field from still being integrated out. This results in an effective Hamiltonian in the excited state along the symmetry line $\epsilon=0$,

$$H = \int_{\mathbf{r}} m[\phi(\mathbf{r}) - 1/2]^2 + u[\phi(\mathbf{r}) - 1/2]^4 - g|\Psi(\mathbf{r})|^2|\phi(\mathbf{r}) - 1/2|$$

where $g = 2\alpha|\eta|$. The mean field approximation can be used to compute the free energy, phase diagram and extent of demixing as done previously in the ground state. For the calculation in **Figure 2** of the main text, we use $g = 0.57 K$, which is arrived at from the polaron binding energy and extent computed from molecular dynamics simulations.

Discretizing the theory to study clustering dynamics

In order to simulate the clustering process, we develop an effective discretized version of the Landau theory outlined above. We do this by making two approximations 1) that the phase separation can be modeled by an Ising model and 2) that the influence of the polaron is to locally renormalize the coupling between the nearest neighbor sites. The Hamiltonian for the model is

$$\mathcal{H} = -\sum_{<ij>} J_{ij} s_i s_j - \lambda \int_r \sum_i \rho(r) s_i \delta(r - r_i)$$

where the sum runs to the N sites, $s_i = \{\pm 1\}$, $\delta(x)$ is Dirac's delta function, and $\boldsymbol{\rho(r)}$ is the polaron density parameterized by a center and a length, l. The density is assumed to have the form

$$\rho(\vec{r}) = \left(\frac{1}{2\pi\ell}\right)^{3/2} e^{-\vec{r}^2/2\ell^2}$$

and the local coupling depends on its location through

$$J_{i,j} = J_o + \Delta \int_r \sum_{i,j} \rho(r) \delta(r - r_{ij})$$

where λ biases the polaron to be in the iodide rich regions.

We associated nearest neighbor swapping between lattice sites to model the diffusion of the halides, and a continuum diffusive dynamics of the excess charge. The characteristic timescales for both of these motions is known experimentally, with halide hopping occurring every 1 ms,[18] and polaron motilities about 1000x faster.[9] The dynamics are propagated with Monte Carlo using standard Metropolis acceptance criteria with the Hamiltonian above.

The parameters used to reproduce the PL intensity as a function of time in **Figure 3b** are, $T=1$, $J_o =0.3$, $\lambda=0.2$, $l=5$, $\Delta=0.5$ with N swap attempts set to a physical time of 1 ms. The system is simulated on circle of radius 50 sites with open boundary conditions. These conditions mimic the strain relaxation at the boundary of the grain, effectively biasing the minority species to the boundary in the demixed phase. To simulate the PL intensity as a function of time, the system is initialized with a uniform spin distribution and the polaron placed in the center of the grain. To converge **Figure 3b**, 10,000 trajectories were averaged.

Electron beam exposure does not cause demixing

The electron beam excitation does not cause demixing because the mode of excitation is not continuous. As the electron beam scans across the sample, the beam dwells on each pixel for ~20 μs before moving to the next pixel. Therefore, excitations are present at each pixel for ~20 μs plus the lifetime of the charge carriers, which is much shorter than the dwell time. According to Figure 3b, this is not nearly enough time to induce cluster formation, which would require the constant replenishing of carriers during steady state (seconds to minutes) illumination. The requirement for the continuous presence of polarons to induce and stabilize iodide-rich clusters has also been demonstrated using a pulsed light source.[20]

Supporting information figures
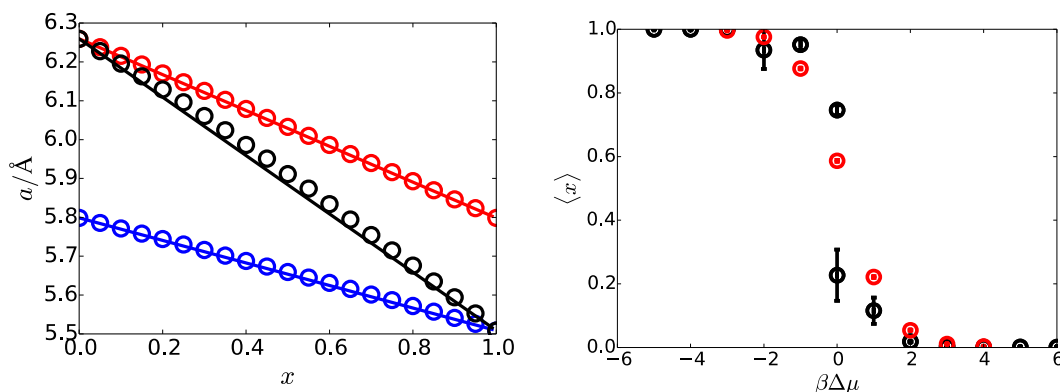
Figure S1. Model validation calculations. (left) Lattice constants as a function of composition for mixtures of Br_xI_{1-x} (red), I_xCl_{1-x} (black), and Br_xCl_{1-x} (blue). (right) Average composition at constant chemical potential difference for mixtures of Br_xI_{1-x} (red), I_xCl_{1-x} (black) While ‹x› changes continuously through $\Delta\mu=0$ for Br_xI_{1-x} mixtures, the abrupt change for I_xCl_{1-x} mixtures reflects its room temperature instability.

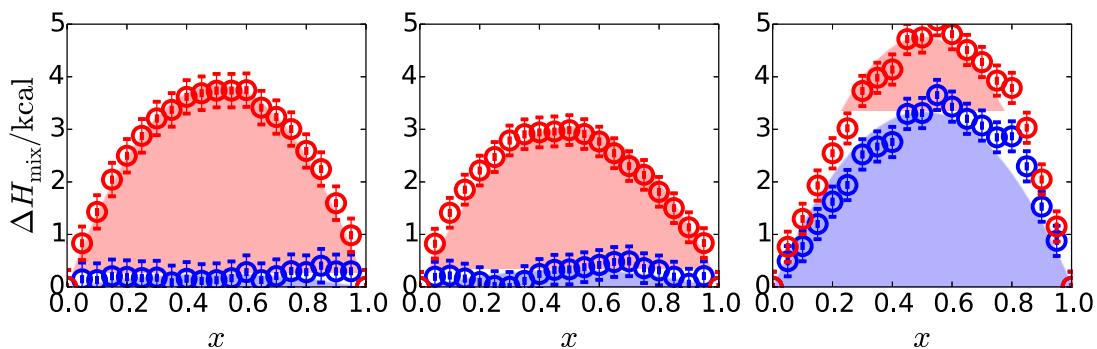**Figure S2.** Excess enthalpies of mixing computed at constant volume (red) or constant stress (blue) for mixtures of (left) Br_xI_{1-x}, (middle) Br_xCl_{1-x}, and (right) I_xCl_{1-x}.
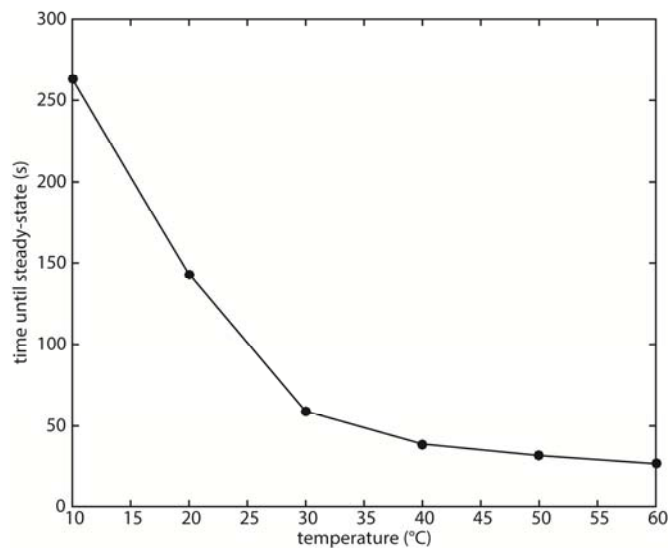

Figure S3. Probing the temperature dependence of phase separation with PL. The time it takes for the PL peak of the iodide-rich clusters to reach a maximum value for a $MAPb(Br_{0.1}I_{0.9})_3$ film at 100 mW/cm^2 as a function of temperature with a 405 nm excitation source.
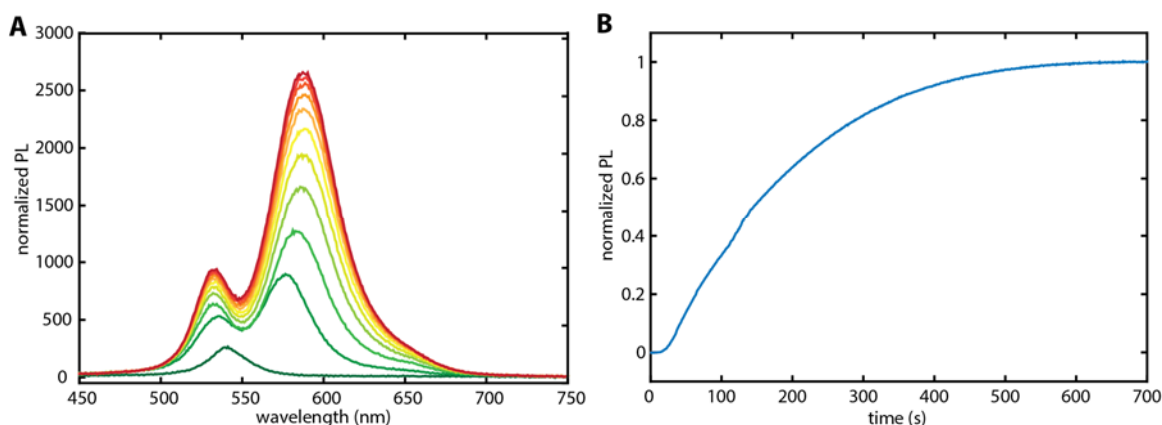
9

Figure S4. PL of CsPb(Br$_{0.1}$I$_{0.9}$)$_3$. (**A**) PL spectra of CsPb(Br$_{0.1}$I$_{0.9}$)$_3$ collected every 1 min at 100 mW/cm^2. (**B**) Normalized PL intensity versus time of the iodide cluster peak. The wavelength shift of the iodide cluster PL peak here is much less significant than that of MAPb(Br$_{0.1}$I$_{0.9}$)$_3$. Furthermore, compared to the normalized PL versus time plot of MAPb(Br$_{0.1}$I$_{0.9}$)$_3$ (Figure 3B), the normalized PL plot of CsPb(Br$_{0.1}$I$_{0.9}$)$_3$ shows that it takes much longer for the iodide cluster peak to saturate.

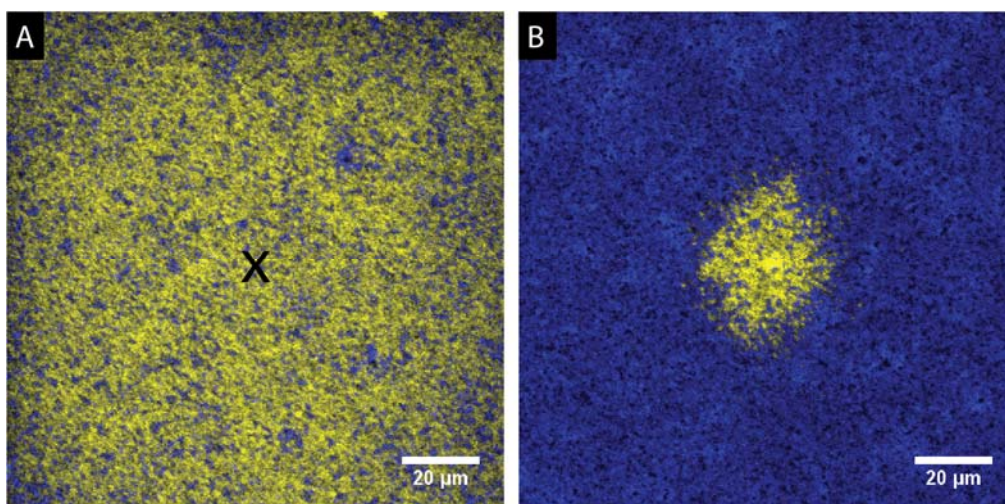**Figure S5. Demonstration that red light can stabilize iodide-rich clusters.** (**A**) Confocal microscopy image of a CH$_3$NH$_3$Pb(I$_{0.1}$Br$_{0.9}$)$_3$ film after light soaking with 405 nm light for 5 minutes. Emission from Br-rich regions (500-550 nm, blue) and I-rich regions (650-750 nm, yellow) are recorded simultaneously. After 5 min, the 405 nm light is turned off and a 635 nm laser is focused on the X. (**B**) After 5 min, an image is recorded with 405 nm excitation. The spot in the middle of the image still emits at 690 nm, confirming that clusters are stabilized by 635 nm light.
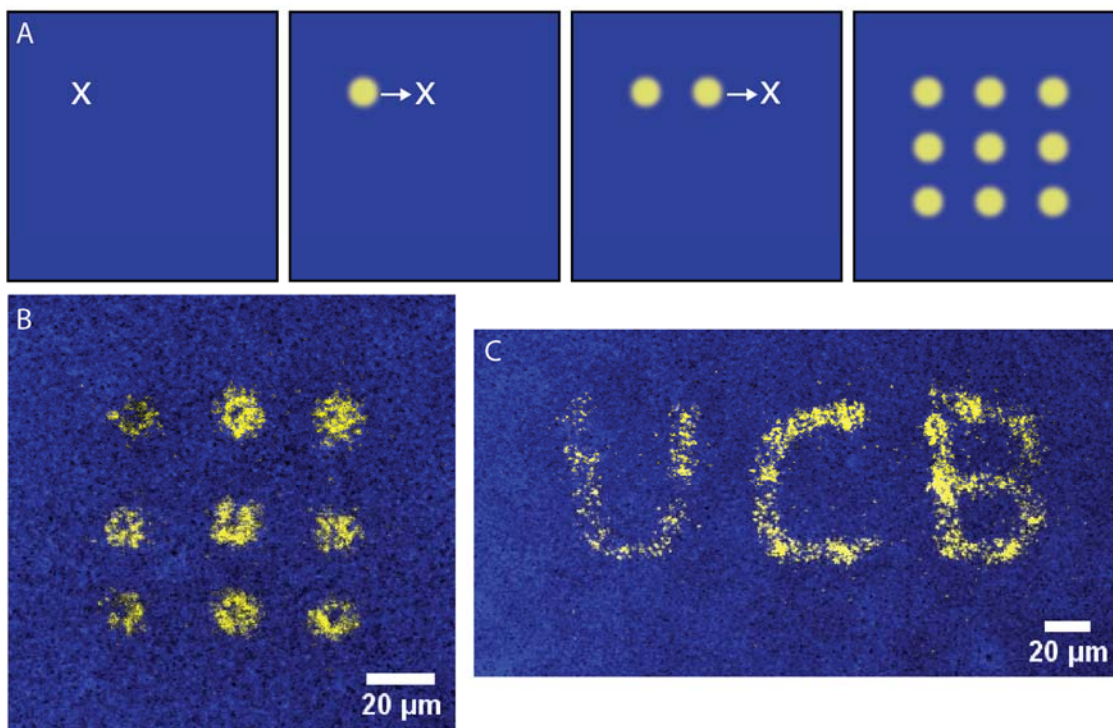
Figure S6. Transiently patterning mixed halide perovskite films. (**A**) Schematic of the series of steps used to generate a pattern in a $CH_3NH_3Pb(I_{0.1}Br_{0.9})_3$ film. I-rich areas are yellow and Br-rich areas are blue. To experimentally achieve this scheme a 660 nm LED illuminates the sample continuously to stabilize any clusters formed with a focused 405 nm laser (white X). This 405 nm laser is scanned to different points to form a 3x3 grid pattern by inducing phase separation at discrete locations. An array of spots (**B**) and an image of 'UCB' (**C**) provide experimental realizations of the scheme, imaged (also using 405 nm excitation) after cluster patterning.
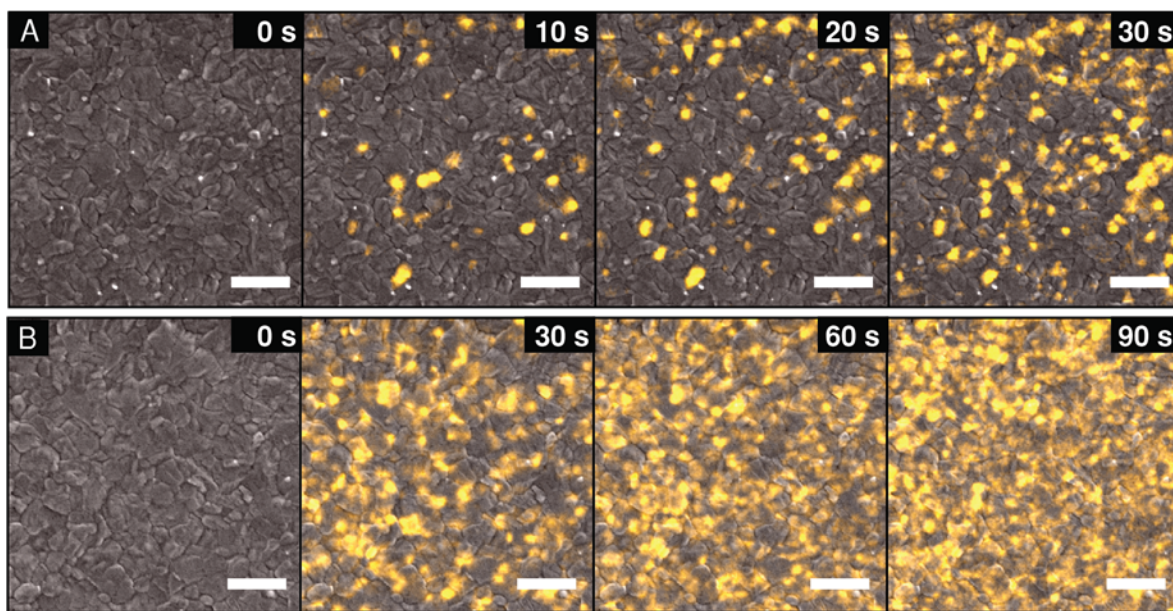
Figure S7. CL images of I-rich cluster formation at 1100 mW/cm². At higher illumination intensity the rate of cluster formation increases because of the increase in number of photogenerated carriers capable of intercepting iodide concentration fluctuations. (**A**) Light soaking for 10 s between CL scans. (**B**) Light soaking for 30 s between CL scans. The scale bars are 2 μm.
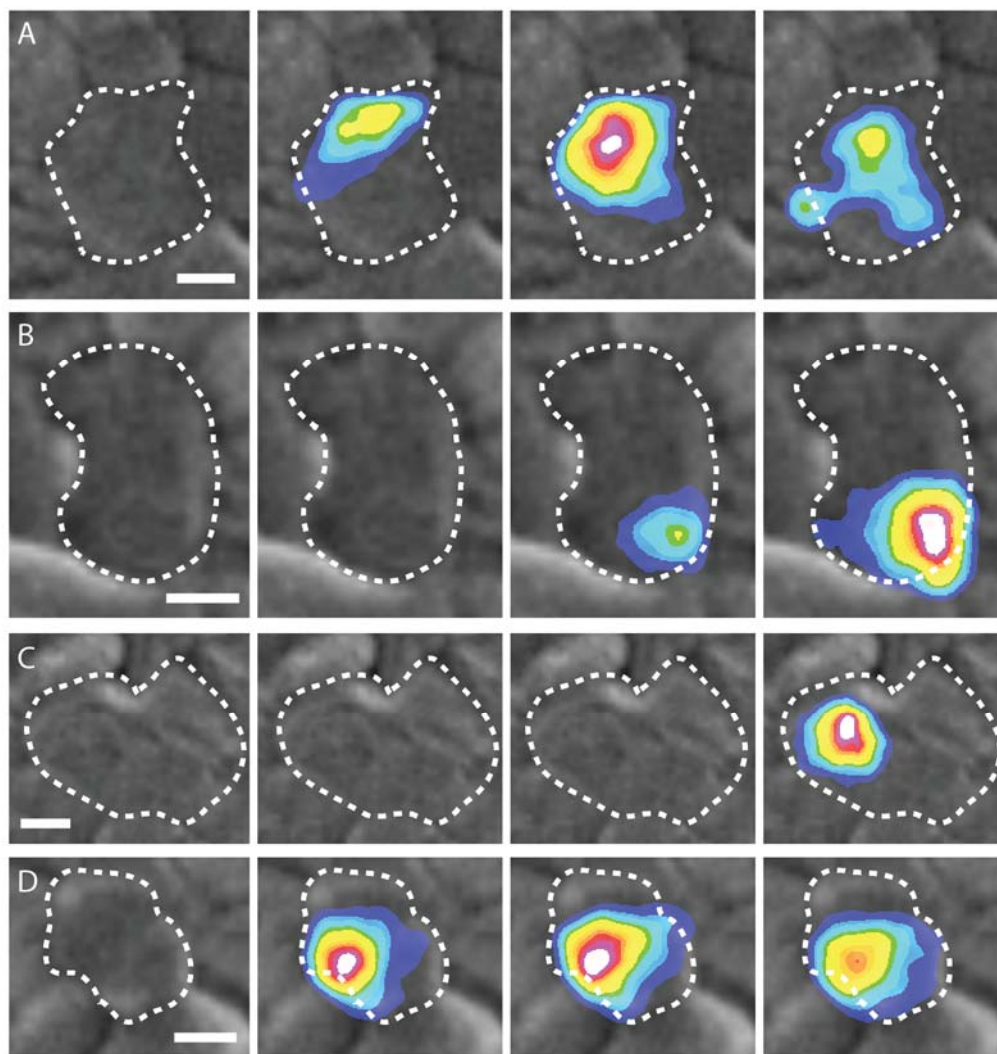
Figure S8. Additional CL data of the formation of iodide-rich clusters. (A-D) Examples of other cluster formation in single domains with 10 seconds of light soaking in between frames. The scale bars are 300 nm.
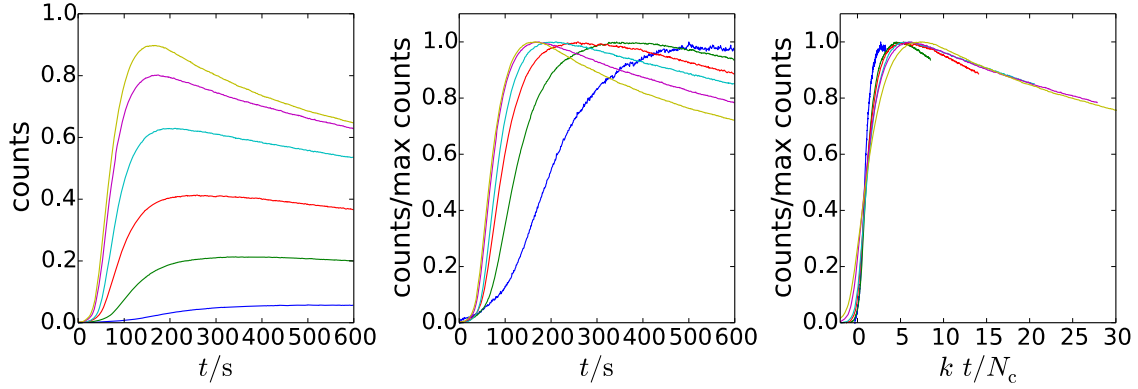
Figure S9. Time dependence of the experimental PL intensity at different illumination intensities. (left) Time dependence of the integrated PL intensity between 600-800 nm for excitation intensities of 4.0, 10, 18, 25, 35, 45, and 55 mW/cm^2. (middle) PL intensity versus time, normalized by respective maxima. (right) PL intensity, normalized by its maximum, versus time scaled by the inverse carrier concentration. The trends in maximum PL intensity and in time for it to be achieved are analyzed in **Figures S11** and **S10**, respectively.
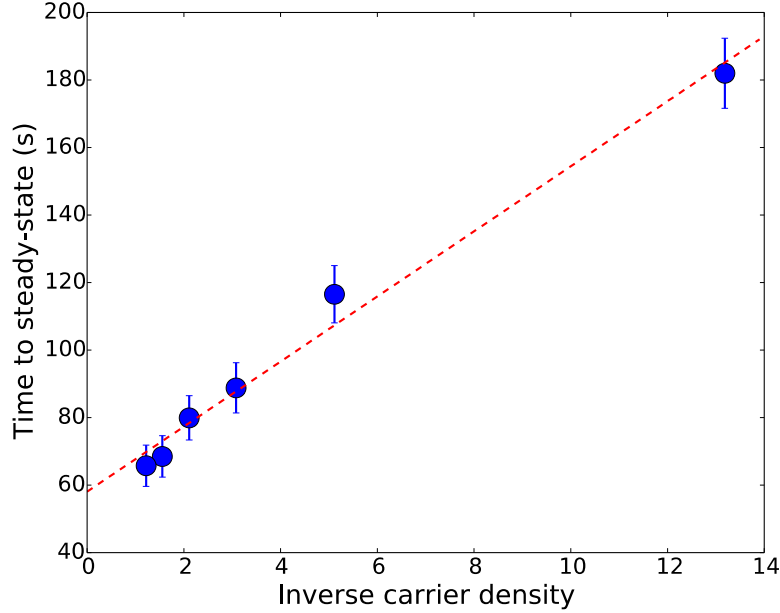

Figure S10. Time to steady state scales linearly with inverse carrier density. An average time to steady state as a function of inverse charge carrier density. The average time is computed by fitting the PL intensity versus time in **Figure S9** to a functional form, $\mathcal{I}(t) = A \tanh((t - \tau)/\delta\tau) + Bt + C$, where τ is taken to be the mean time to steady state and $\delta\tau^{1/2}$ is used as the error.
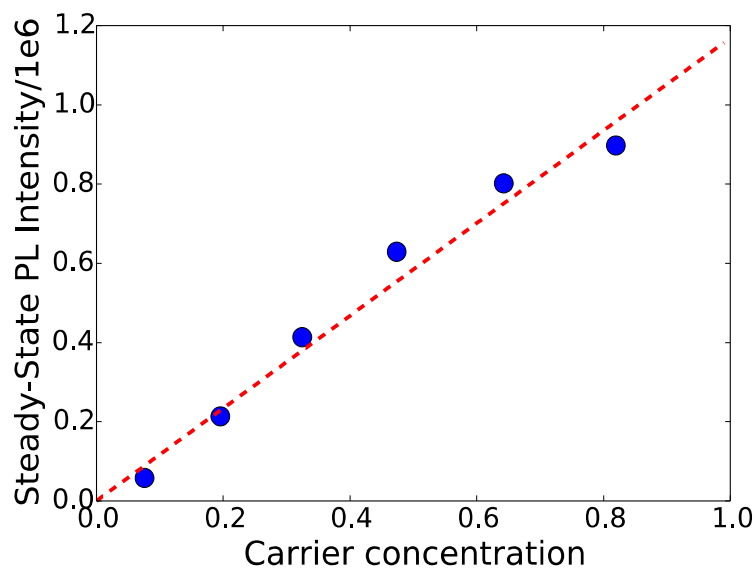
14

Figure S11. Steady state amount of iodide-rich composition is proportional to carrier concentration. Maximum PL intensity from **Figure S9** as a function of carrier concentration. Assuming each cluster is equally luminescent, and that the clusters are spherical on average, the linear relationship allows us to extract a mean cluster size referenced in the main text.
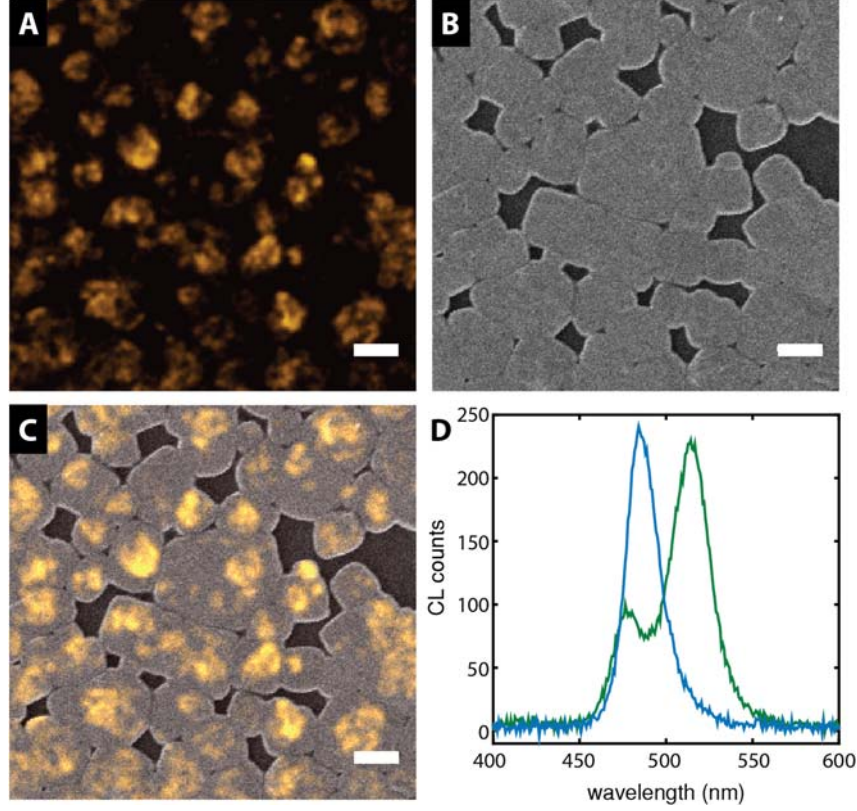
Figure S12. Light-induced halide phase separation in a MAPb(Br$_{0.5}$Cl$_{0.5}$)$_3$ film. (A) CL image (509 nm longpass filter), (**B**) SE image, and (**C**) CL/SE overlay of a MAPb(Br$_{0.5}$Cl$_{0.5}$)$_3$ film after 1 min light soaking at 100 mW/cm^2. Scale bars are 1.0 μm. (**D**) CL spectra before (blue) and after (green) light soaking.
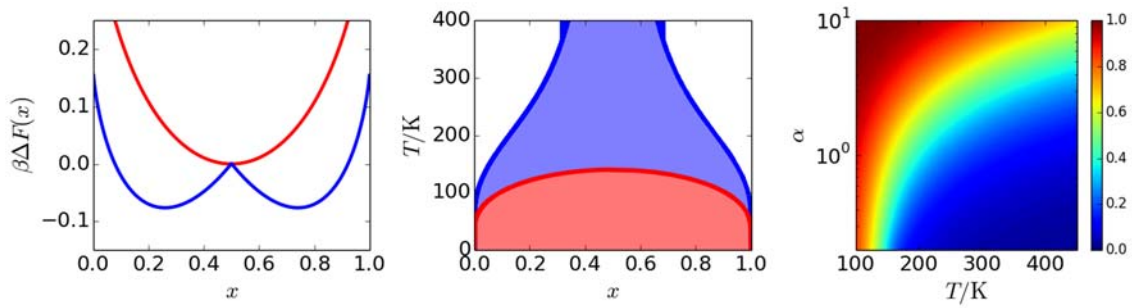
Figure S13. Free energies and phase behavior for Br/Cl mixtures. Using $m = 2T(K)-280K$, as computed from the molecular dynamics simulations, and the same g used in the Br/I case, we construct the free energies, phase diagrams and extents of demixing for solid solutions of Br/Cl. (left) Free energy per unit cell computed from mean field theory in the ground (red) and photo-excited (blue) states. (middle) Phase diagram in the ground (red) and excited (blue) states. (right) Extent of demixing as a function of electron-phonon coupling.

Supporting video captions

Video S1. Molecular dynamics simulation of a 99% isosurface of excess charge density on the perovskite lattice.

Video S2. Sequence of CL images of phase separation with 10 s light soaking intervals at 50 mW/cm^2. Movie of the CL images shown in Figure 3A.

Video S3. Sequence of CL images of phase separation with 30 s light soaking intervals at 50 mW/cm^2. Movie of the CL images shown in Figure 3B.

Video S4. Sequence of CL images of phase separation with 10 s light soaking intervals at 1100 mW/cm^2. Movie of the CL images shown in Figure S7A.

Video S5. Sequence of CL images of phase separation with 30 s light soaking intervals at 1100 mW/cm^2. Movie of the CL images shown in Figure S7B.

Video S6. Cluster formation simulation. Movie of a cluster formation simulation with iodide-rich regions in yellow and bromide-rich regions in blue.

Supporting Tables

Table S1a: Buckingham potential parameters

Pair	A (kcal/mol)	ρ (Å)	C (Å^6 kcal/mol)	Pair	A (kcal/mol)	ρ (Å)	C (Å^6 kcal/mol)
Pb-Pb	70359906	0.131258	0	I-C	112936	0.342426	0
Pb-I	103496	0.321737	0	I-N	112936	0.342426	0
Pb-Br	103496	0.30368	0	Br-Br	22793	0.42961	696.9495
Pb-Cl	103496	0.2917	0	Br-Cl	22793	0.4126616	696.9495
Pb-C	32690390	0.150947	0	Br-C	112936	0.323208	0
Pb-N	32690390	0.150947	0	Br-N	112936	0.323208	0
I-I	22793	0.482217	696.9495	Cl-Cl	22793	0.3963	696.9495
I-Br	22793	0.45515	696.9495	Cl-C	112936	0.3104578	0
I-Cl	22793	0.437198	696.9495	Cl-N	112936	0.3104578	0

Table S1b: Lennard Jones parameters

Pair	ϵ (kcal/mol)	σ (Å)
Pb-H_1	0.0140	2.26454
Pb-H_2	0.0140	2.70999
I-H_1	0.574	2.75
I-H_2	0.574	3.10
Br-H_1	0.574	2.5957
Br-H_2	0.574	2.9260
Cl-H_1	0.574	2.4932
Cl-H_2	0.574	2.8105
C-H_1	0.0414	2.23440
C-H_2	0.0414	2.6798
N-H_1	0.0517	2.1595
N-H_2	0.0517	1.069

Table S1c: Partial Charges Used

Species	Pb	I/Br/Cl	C	N	H_1	H_2
q	2.030000	-1.130000	0.771000	-1.100000	0.540000	0.023000

Table S2: Short range cutoffs

Species	Pb	C	H_1	H_2
R/Å	3.1	1.1	1.0	1.0

Supporting Information References

(1) Jang, D. M.; Park, K.; Kim, D. H.; Park, J.; Shojaei, F.; Kang, H. S.; Ahn, J.-P.; Lee, J. W.; Song, J. K. *Nano Lett.* **2015**, *15* (8), 5191–5199.

(2) Mattoni, A.; Filippetti, A.; Saba, M. I.; Delugas, P. *J. Phys. Chem. C* **2015**, *119* (30), 17421–17428.

(3) Lewis, G. V.; Catlow, C. R. A. *J. Phys. C Solid State Phys.* **1985**, *18* (6), 1149.

(4) Parrinello, M.; Rahman, A. *J. Appl. Phys.* **1981**, *52* (12), 7182–7190.

(5) Zhang; Glotzer, S. C. *Nano Lett.* **2004**, *4* (8), 1407–1413.

(6)   Mashiyama, H.; Kurihara, Y.; Azetsu, T. *J.- Korean Phys. Soc.* **1998**, *32*, S156–S158.

(7)   Plimpton, S. *J. Comput. Phys.* **1995**, *117* (1), 1–19.

(8)   Rakita, Y.; Cohen, S. R.; Kedem, N. K.; Hodes, G.; Cahen, D. *MRS Commun.* **2015**, *5* (4), 623–629.

(9)   Poglitsch, A.; Weber, D. *J. Chem. Phys.* **1987**, *87* (11), 6373–6378.

(10)   Chandler, D.; Wolynes, P. G. *J. Chem. Phys.* **1981**, *74* (7), 4078–4095.

(11)   Chandler, D.; Singh, Y.; Richardson, D. M. *J. Chem. Phys.* **1984**, *81* (4), 1975–1982.

(12)   Parrinello, M.; Rahman, A. *J. Chem. Phys.* **1984**, *80* (2), 860–867.

(13)   Kumar, S.; Rosenberg, J. M.; Bouzida, D.; Swendsen, R. H.; Kollman, P. A. *J. Comput. Chem.* **1992**, *13* (8), 1011–1021.

(14)   Cahn, J. W. *Acta Metall.* **1961**, *9* (9), 795–801.

(15)   Chaikin, P. M.; Lubensky, T. C. *Principles of Condensed Matter Physics*; Cambridge University Press: Cambridge; New York, NY, USA, 2000.

(16)   Whitfield, G.; Shaw, P. B. *Phys. Rev. B* **1976**, *14* (8), 3346–3355.

(17)   Kalosakas, G.; Aubry, S.; Tsironis, G. P. *Phys. Rev. B* **1998**, *58* (6), 3094–3104.

(18)   Eames, C.; Frost, J. M.; Barnes, P. R. F.; O'Regan, B. C.; Walsh, A.; Islam, M. S. *Nat. Commun.* **2015**, *6*, 7497.

(19)   Stranks, S. D.; Eperon, G. E.; Grancini, G.; Menelaou, C.; Alcocer, M. J. P.; Leijtens, T.; Herz, L. M.; Petrozza, A.; Snaith, H. J. *Science* **2013**, *342* (6156), 341–344.

(20)   Yang, X.; Yan, X.; Wang, W.; Zhu, X.; Li, H.; Ma, W.; Sheng, C. *Org. Electron.* **2016**, *34*, 79–83.